

WAM-Nav: Asymmetric Latent World-Action Modeling for Unified Visual Navigation

Ning Yang^{1,2}, Yan Huang^{2,3,4,*}, Kaiwen Peng^{2,3}, Ziheng He^{2,3},
Kai Wang^{2,3}, Cui Miao⁵, Kailin Lyu^{2,3}, Guo Li⁶,
Xiaofeng Wang^{6,7}, Zheng Zhu⁷, Jing Liu⁵, Nianfeng Liu⁵

¹Nanjing University ²Institute of Automation, Chinese Academy of Sciences
³University of Chinese Academy of Sciences ⁴FiveAges
⁵National University of Defense Technology ⁶Tsinghua University ⁷GigaAI

Abstract: Visual navigation requires generating smooth and collision-free trajectories under complex geometric and physical constraints. Existing reactive policies that directly map observations to actions lack anticipatory reasoning, limiting their ability to proactively avoid obstacles. While visual imagination offers predictive foresight, conventional modular approaches separate scene prediction from policy learning, often leading to error accumulation and inefficient inference. To address these limitations, we propose WAM-Nav, a Latent World-Action Model for embodied visual navigation that jointly learns action generation and latent visual foresight, enabling more robust and foresighted navigation decisions without compromising inference efficiency. Specifically, WAM-Nav utilizes a shared Diffusion Transformer for asymmetric joint diffusion to concurrently generate long-horizon actions and short-horizon visual foresight, reducing the inference latency and visual error accumulation inherent in multi-step autoregressive rollouts. To further encourage smooth and consistent trajectory generation, we introduce a dual-stream contextual conditioning mechanism that integrates episode-level ego-motion history with sequential visual observations. Combined with a unified goal alignment module that preserves balanced representations across goal types, WAM-Nav naturally supports Image-Goal, Point-Goal, and No-Goal exploration within a single policy. Extensive experiments on the challenging *ClutterScenes* and *InternScenes* benchmarks demonstrate strong generalization of WAM-Nav, particularly on Image-Goal and Point-Goal navigation, where it improves success rates by **15.7%** and **3.3%**, respectively. Real-world deployment further validates effective zero-shot sim-to-real transfer, achieving an average **85%** task success rate across diverse indoor and outdoor environments.

Keywords: Embodied Visual Navigation, World-Action Model, Diffusion Transformer

1 Introduction

Embodied visual navigation [1, 2, 3, 4] aims to guide agents through complex, unseen physical environments by generating smooth, collision-free trajectories based on visual observations [5]. Over the past few years, the dominant navigation paradigm has gradually transitioned from traditional decoupled mapping-and-planning pipelines [6, 7, 8] to learning-based intelligent methods. As shown in Figure 1 (a), recent end-to-end reactive approaches [9, 10, 11, 12, 13] directly map visual observations to executable actions. Moreover, to endow agents with predictive reasoning capabilities, recent research has actively explored visual imagination and world-model-based navigation strategies. These modular approaches generally fall into two distinct paradigms. The first paradigm

* Corresponding author.

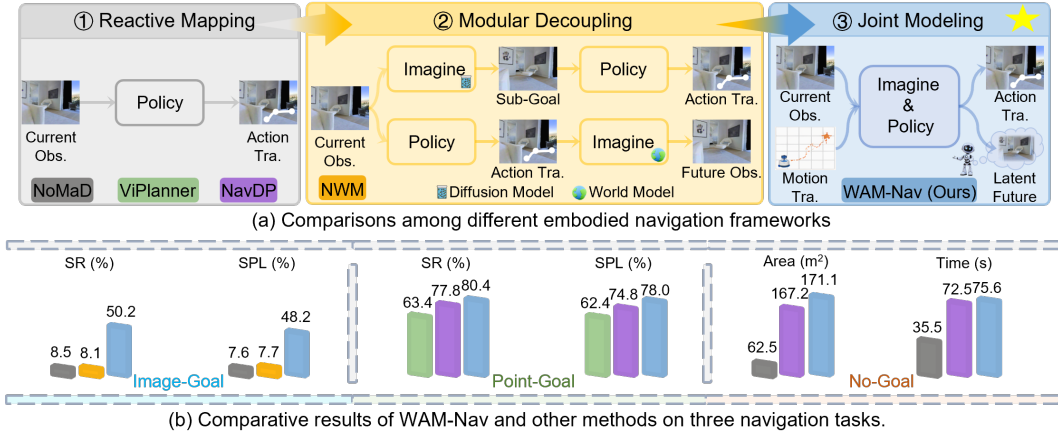


Figure 1: Overview of the WAM-Nav paradigm and performance. (a) Methodological comparison: Unlike traditional purely reactive or decoupled modular pipelines, WAM-Nav jointly models action generation and latent visual foresight within a unified framework. (b) Quantitative performance: Our method achieves competitive results against established baselines across diverse evaluation settings.

prioritizes generating future visual subgoals, which are subsequently utilized to infer control actions via inverse dynamics models [14, 15]. The second paradigm focuses on trajectory evaluation, where candidate paths are first generated and then scored by a world model that imagines future visual states [16, 17, 18].

Although existing approaches have improved robotic navigation to varying degrees, fundamental limitations remain across current paradigms. Reactive end-to-end mapping methods, which directly map observations to actions, rely heavily on instantaneous perception and therefore lack predictive reasoning and local dynamics understanding, making them prone to local optima and collisions in cluttered environments. Modular decoupled approaches provide explicit foresight, but their separate training of action decision-making and future imagination introduces substantial computational latency and compounding errors, often resulting in delayed responses and poor trajectory consistency. While existing World-Action Models have shown promising joint visual-action modeling capabilities in robot manipulation [19, 20, 21], their autoregressive generation paradigm remains challenging for navigation due to limited real-time capability and accumulated prediction errors under large viewpoint changes. Furthermore, most existing navigation methods are designed for a single target specification [9, 10, 11, 12, 16, 14, 18], requiring redesign, new data collection, and retraining when adapting to new tasks. Although NavDP [13] supports multiple goal-oriented navigation tasks, its unimodal alignment design still leads to imbalanced performance across task types.

Motivated by these advances, we propose WAM-Nav, a Latent World-Action Model for embodied visual navigation that jointly learns action generation and latent visual foresight, enabling more robust and foresighted navigation decisions without compromising inference efficiency, as illustrated in Figure 1. Instead of relying on sequential decoupled modules, WAM-Nav utilizes a shared Diffusion Transformer (DiT) for asymmetric joint diffusion to concurrently generate long-horizon actions and short-horizon visual foresight. This joint modeling reduces the inference latency and visual error accumulation inherent in multi-step autoregressive rollouts, while ensuring a deep coupling between visual features and control dynamics to empower the policy to anticipate environmental variations and proactively steer clear of obstacles. To further guide generation and preserve trajectory consistency, we introduce Dual-Stream Contextual Conditioning (DSCC), which integrates episode-level ego-motion history with sequential visual observations. Combined with a unified goal alignment module that preserves balanced representations across goal types, WAM-Nav naturally supports Image-Goal, Point-Goal, and No-Goal exploration within a single policy without complex architecture switching. We conduct extensive evaluations on cluttered and physically realistic benchmarks, including the *ClutterScenes* and *InternScenes*. Experimental results demonstrate that WAM-Nav achieves strong zero-shot generalization, particularly on Image-Goal and Point-Goal navi-

gation where it improves success rates by **15.7%** and **3.3%**, respectively. Furthermore, deployment on physical robot platforms validates its capability for sim-to-real transfer, achieving an average **85%** task success rate across diverse indoor and outdoor environments.

2 Related Work

2.1 Learning-based Embodied Visual Navigation

In contrast to traditional mapping-and-planning methods, the end-to-end learning framework has emerged as a dominant paradigm for embodied visual navigation [5, 22, 23, 24, 25]. Recent foundation models have significantly advanced this field: GNM [9] demonstrated cross-embodiment generalization using a lightweight CNN policy [26], while ViNT [10] extended navigation horizons via Transformer-based sub-goal planning. Subsequently, NoMaD [11] introduced diffusion policies [27] to model multi-modal action distributions, and NavDP [13] incorporated an actor-critic mechanism to score and select the safest generated trajectories. Despite these advances, such reactive policies directly map local observations to actions without explicitly modeling their future perceptual consequences, rendering them susceptible to collisions in cluttered environments [14, 28]. In contrast, WAM-Nav addresses this limitation by integrating predictive visual foresight directly into the policy, enabling proactive obstacle avoidance and safer navigation decision-making.

2.2 World Models and Visual Imagination for Navigation

Integrating visual imagination facilitates foresight-driven navigation [29, 30], and early systems typically adopt modular architectures to evaluate candidate motions. For instance, Pathdreamer [31] and NWM [16] rely on decoupled visual prediction and trajectory planning, synthesizing future observations via a world model built atop an existing navigation policy. Similarly, NavigateDiff [14] employs diffusion models [32] to imagine future visual sub-goals, which are subsequently executed by a separate inverse dynamics policy. These approaches treat visual imagination and trajectory generation as sequential and decoupled processes. This separation frequently introduces state-action misalignment and compounding control errors. In response, WAM-Nav jointly models action generation and visual foresight, where future visual dynamics are predicted in a latent space. Rather than decoupling prediction from decision-making, it learns both jointly to promote temporal consistency and physical feasibility with minimal inference latency.

3 Methodology

As illustrated in Figure 2, WAM-Nav consists of three key components: (1) *Unified Goal Alignment*, (2) *Dual-Stream Contextual Conditioning*, and (3) *Asymmetric Action-Foresight Generation*. Specifically, to enable balanced performance across diverse navigation tasks, we first project heterogeneous goal specifications into a unified alignment space. We then construct a dual-stream spatiotemporal context by jointly encoding the robot’s sequential visual observations and episode-level ego-motion history. Both streams are explicitly modulated by goal-relevant information and aggregated into a compact conditioning context C . Conditioned on C , a shared DiT jointly generates future action trajectories and latent visual foresight through asymmetric denoising.

3.1 Unified Goal Alignment

To enable balanced performance across Image-Goal, Point-Goal, and No-Goal exploration within a single policy, WAM-Nav introduces a unified goal alignment mechanism. Unlike prior navigation approaches [13, 33] that reformulate all tasks as point-goal navigation, our design preserves modality-specific goal information to maintain task-specific expressiveness across different navigation settings. Given a goal input g , WAM-Nav encodes it into two complementary goal embeddings: a visual semantic query $g_V \in \mathbb{R}^D$ for visual memory retrieval, and a geometric query $g_G \in \mathbb{R}^D$ for trajectory-level directional guidance.

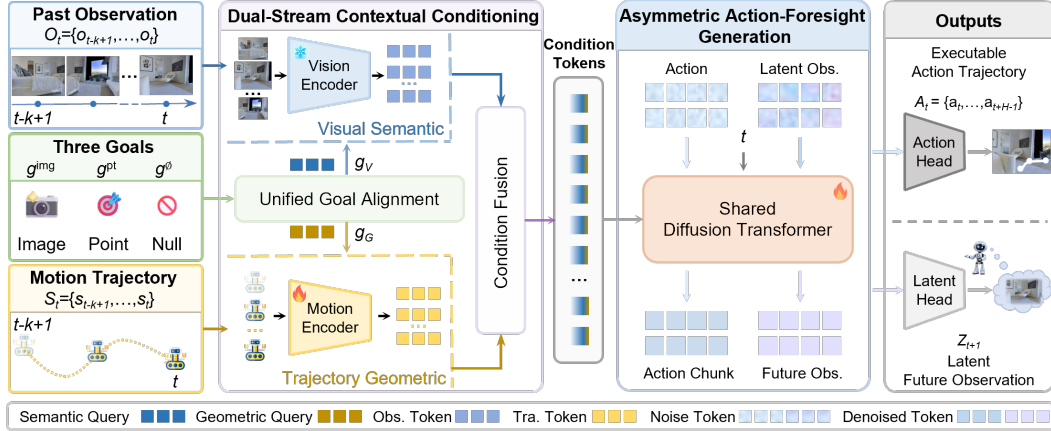


Figure 2: Architecture overview of the WAM-Nav framework. Heterogeneous navigation goals are explicitly routed into visual-semantic (g_V) and trajectory geometric (g_G) queries. These queries contextually modulate historical RGB-D sequences and relative ego-motion trajectories, synthesizing a compact conditioning context C . Conditioned on C , a shared DiT performs asymmetric joint generation of future control actions and latent visual foresight.

Formally, the goal input g is first transformed into a base embedding e_g via a modality-specific feature extractor $E_\phi(\cdot)$, and then projected into the two functional token spaces:

$$g_V = \psi_V(e_g), \quad g_G = \psi_G(e_g), \quad \text{with } e_g = E_\phi(g) \quad (1)$$

where $E_\phi(\cdot)$ is instantiated according to the goal modality, including a Vision Transformer trained from scratch for image goals, sinusoidal positional encoding for relative coordinates, and a masked zero-state representation for goal-free exploration. The projection operators $\psi_V(\cdot)$ and $\psi_G(\cdot)$ are learnable linear mappings that map the base embedding into the visual semantic and geometric spaces, respectively.

This alignment design preserves modality-specific goal information while providing a unified interface across heterogeneous navigation tasks, enabling balanced performance across different goal settings and producing goal-conditioned context for the subsequent Section 3.2, where it serves as conditioning for the joint modeling of action and visual foresight.

3.2 Dual-Stream Contextual Conditioning

While visual history provides spatial cues for obstacle avoidance, relying solely on visual conditioning often leads to kinematically inconsistent or jittery trajectories due to the lack of explicit momentum constraints. To address this, WAM-Nav introduces Dual-Stream Contextual Conditioning (DSCC) over a historical sliding window from $t - k + 1$ to t . We dynamically construct the conditioning context C by fusing a goal-modulated visual memory stream (capturing local spatial geometry) with a trajectory-aware kinematic history stream (capturing physical momentum). Fusing these streams provides the shared DiT with a spatiotemporal conditioning context that ensures the generated action trajectories are both geometrically collision-free and kinematically smooth.

Goal-Modulated Visual Memory. Historical RGB observations \mathcal{O}_t are processed by DINO-v2 [34] into a memory tensor $V \in \mathbb{R}^{B \times (k \cdot P) \times D}$, where B represents the batch size, k is the historical window length, and P is the patch count per frame. To selectively reinforce spatial tokens relevant to the target, the visual query $g_V \in \mathbb{R}^{B \times D}$ computes independent relevance scores for each patch token via a scaled dot-product:

$$\alpha = \sigma \left(\frac{g_V V^\top}{\sqrt{D}} \right) \in \mathbb{R}^{B \times (k \cdot P) \times 1} \quad (2)$$

where σ is the sigmoid function. The visual memory is then residually updated:

$$\tilde{V} = V + \alpha \odot V \quad (3)$$

Trajectory-Aware Motion History. To incorporate the agent’s kinematic momentum and ensure robust zero-shot generalization, the motion trajectory stream processes the executed pose sequence \mathcal{S}_t . Absolute poses are converted into coordinate-invariant relative displacements and heading changes in the current egocentric frame, yielding a relative kinematics sequence $\tilde{\mathcal{S}}_t = \{(\Delta x_i, \Delta y_i, \Delta \theta_i)\}_{i=t-k+1}^t$ (detailed in Appendix C.1).

This relative motion sequence $\tilde{\mathcal{S}}_t$ is embedded and processed by a causal Transformer encoder $H \in \mathbb{R}^{B \times k \times D}$ to capture temporal kinematic profiles. To align past momentum with current target directionality, we query H with the geometric goal embedding $g_G \in \mathbb{R}^{B \times D}$ via cross-attention to extract a consolidated kinematic vector o_{kin} :

$$o_{\text{kin}} = \text{CrossAttn}(g_G, H, H) \in \mathbb{R}^{B \times D} \quad (4)$$

The vector o_{kin} mathematically summarizes the agent’s historical motion continuity relative to its target directionality.

Condition Fusion via Cross-Attention. To structurally enforce kinematic momentum to guide spatial visual retrieval, the visual and trajectory streams are integrated via a multi-layer Transformer Decoder to formulate the unified conditioning context $C \in \mathbb{R}^{B \times N_c \times D}$. Specifically, the extracted kinematic token o_{kin} is projected to bias a set of learnable query embeddings $Q_c \in \mathbb{R}^{N_c \times D}$:

$$C = \text{TransformerDecoder}\left(Q_c + \phi(o_{\text{kin}}), \tilde{V}, \tilde{V}\right) \quad (5)$$

where $\phi(\cdot)$ denotes a linear projection. Architecturally, this fusion mechanism utilizes the agent’s kinematic momentum (o_{kin}) to actively query the goal-modulated visual spatial context (\tilde{V}). The resulting conditioning context C thus explicitly constrains the subsequent latent generation, enforcing both physical execution smoothness and geometric safety.

3.3 Asymmetric Action-Foresight Generation

Conditioned on the unified conditioning context C , WAM-Nav jointly models the future action trajectory $\mathbf{A}_t = \{a_t, \dots, a_{t+H_{\text{act}}-1}\}$ over a long planning horizon H_{act} and its corresponding latent visual foresight $\mathbf{Z}_{t+1:t+H_{\text{vis}}} = \{z_{t+1}, \dots, z_{t+H_{\text{vis}}}\}$ over a short prediction horizon H_{vis} ($H_{\text{vis}} \leq H_{\text{act}}$) within a shared representation space. The future visual state $z_i = \mathcal{E}(o_i)$ is compressed via a pre-trained Stable Diffusion VAE [35] into a compact grid of N latent patches.

To optimize this generative process, we employ the flow-matching [36] training strategy to learn the joint conditional distribution $p_\theta(\mathbf{A}, \mathbf{Z} \mid C)$ via asymmetric joint diffusion. This strategy formulates the continuous probability paths as straight lines that map standard Gaussian priors $(\mathbf{A}_0, \mathbf{Z}_0) \sim \mathcal{N}(\mathbf{0}, \mathbf{I})$ to the empirical data manifold. At any flow time $\tau \in [0, 1]$, the interpolated states are defined as:

$$\mathbf{A}_\tau = (1 - \tau)\mathbf{A}_0 + \tau\mathbf{A}_1, \quad \mathbf{Z}_\tau = (1 - \tau)\mathbf{Z}_0 + \tau\mathbf{Z}_1 \quad (6)$$

where the corresponding target velocity fields are given by $u_A = \mathbf{A}_1 - \mathbf{A}_0$ and $u_Z = \mathbf{Z}_1 - \mathbf{Z}_0$.

The architectural backbone for this asymmetric generative progress is a shared DiT. The noised sequences \mathbf{A}_τ and \mathbf{Z}_τ are tokenized, concatenated, and processed through a multi-layer DiT. Crucially, within each DiT block, these heterogeneous tokens undergo a shared self-attention, enabling the dynamic exchange of spatiotemporal constraints between the physical action paths and the latent visual representations at every layer. Both streams cross-attend to the conditioning context C , with the timestep τ modulated via adaptive LayerNorm (adaLN) layers to regress the joint velocity fields:

$$\hat{u}_A, \hat{u}_Z = f_\theta(\mathbf{A}_\tau, \mathbf{Z}_\tau, \tau, C). \quad (7)$$

This shared parameterization makes latent foresight act as a perception-grounded constraint on action generation, penalizing action–scene inconsistency through the visual velocity-matching loss. Unlike manipulation-oriented WAMs [19, 20], where future visual changes are often local and object-centric, navigation involves large egocentric viewpoint changes; long autoregressive visual rollouts would introduce both inference latency and accumulated visual errors that may misguide action generation. WAM-Nav therefore adopts an asymmetric design: long-horizon actions preserve trajectory continuity, while short-horizon latent foresight provides reliable near-future geometric constraints without overextending visual prediction.

3.4 Model Training and Inference

We train WAM-Nav end-to-end by minimizing a joint objective consisting of flow-matching velocity regression and multi-modal goal alignment:

$$\mathcal{L}_{\text{total}} = \mathbb{E}_{\tau, \mathbf{A}_0, \mathbf{Z}_0} [\|\hat{u}_A - u_A\|_2^2 + \lambda_{\text{img}} \|\hat{u}_Z - u_Z\|_2^2] + \lambda_{\text{align}} \mathcal{L}_{\text{align}} \quad (8)$$

where $\tau \sim \mathcal{U}(0, 1)$, and $\lambda_{\text{img}}, \lambda_{\text{align}}$ are scalar weighting coefficients. The term $\mathcal{L}_{\text{align}}$ represents a symmetric contrastive InfoNCE loss [37]. By maximizing the mutual information between cross-space projections of equivalent objectives, this alignment constraint ensures consistency across diverse goal modalities, facilitating the extraction of unified directional and visual cues regardless of the original input format.

During online deployment, WAM-Nav follows a receding-horizon control loop. Consistent with NAVDP [13], at each step, conditioned on the current conditioning context C , the policy samples 16 candidate trajectories. Following prior generative navigation policies [11], the first sampled trajectory is selected for execution.

4 Experimental Results

We conduct extensive zero-shot deployments of WAM-Nav to evaluate its effectiveness, focusing on five research questions: **Q1:** Does WAM-Nav achieve superior zero-shot generalization while maintaining balanced performance across diverse navigation tasks? **Q2:** What mechanisms enable WAM-Nav to navigate highly cluttered environments more effectively than existing baselines? **Q3:** How computationally efficient is WAM-Nav, and can it meet the real-time requirements of online navigation? **Q4:** How do the individual components contribute to the overall performance improvement? **Q5:** Can WAM-Nav transfer to physical platforms for zero-shot real-world navigation?

4.1 Simulation Experiments

Training Datasets and Setup. Consistent with prior works [12, 13], WAM-Nav is trained on the large-scale visual navigation dataset VLN-N1 [33, 38]. VLN-N1 is built upon six categories of 3D scene assets, including Replica [39], Matterport3D [40], Gibson [41], 3D-FRONT [42], HSSD [43], and HM3D [44]. Leveraging an extensive domain randomization pipeline, the dataset provides over 400 hours of collision-free and smooth first-person navigation trajectories collected in simulation, comprising more than 200K trajectories in total. WAM-Nav is trained with a learning rate of 1.5×10^{-4} and the total training cost is approximately 8×120 GPU hours. Additional implementation details are provided in Appendix D.

Zero-Shot Evaluation Platform. We evaluate WAM-Nav and all baselines in a zero-shot setting on a simulation benchmark built upon IsaacSim, using the wheeled robot ClearPath Dingo as the navigator. All methods are directly evaluated with their original pretrained weights, without additional finetuning. The benchmark includes two categories of environments: *ClutterScenes* and *InternScenes* [13, 33, 45]. The *ClutterScenes* contain 10 *easy* scenes and 10 *hard* scenes. Both are constructed from randomly generated layouts with cluttered obstacles, while the *hard* scenes feature denser obstacle distributions. The *InternScenes* include 20 *home* scenes and 20 *commercial* scenes. *Home* scenes are characterized by narrow passages and cluttered layouts, whereas *commercial* scenes cover representative indoor categories such as *supermarkets* and *restaurants*. For each scene, we randomly sample 100 navigation episodes, yielding a total of 6,000 evaluation episodes.

Metrics. For Image-Goal and Point-Goal navigation, we evaluate **Success Rate (SR)** and **Success weighted by Path Length (SPL)** to measure task completion and navigation efficiency. For No-Goal exploration, we report episode **Time** and explored **Area** to evaluate exploration capability. Episode **Time** is capped at 120 seconds, and episodes that become locally stuck are terminated early. Higher values indicate better performance for all metrics.

Compared Methods.

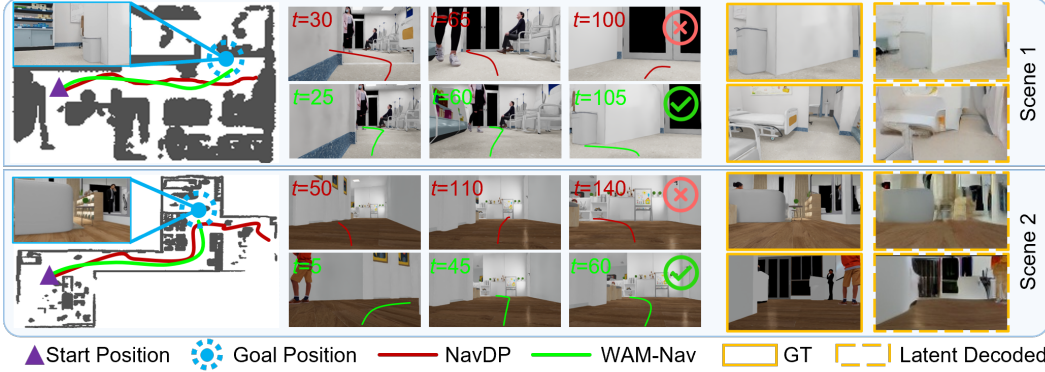


Figure 3: **Qualitative comparison on image-goal navigation.** As shown in the 2D top-down trajectories and egocentric path projections, compared with NavDP, WAM-Nav exhibits smoother, more consistent trajectories and better real-time obstacle avoidance predictions. Despite generating future states entirely in a compressed latent space, its decoded visual foresights remain highly faithful to ground-truth (GT) observations.

To comprehensively evaluate the effectiveness of WAM-Nav, we benchmark our model against a diverse set of strong baselines tailored to different navigation tasks. Specifically, for **Image-Goal** navigation, we compare WAM-Nav against GNM [9], ViNT [10], NoMaD [11], NWM [16], and NavDP [13]. For **Point-Goal** navigation, the baselines include DD-PPO [24], iPlanner [46], ViPlanner [47], and NavDP [13]. Finally, for **No-Goal** exploration, we compare against GNM [9], ViNT [10], NoMaD [11], and NavDP [13] (detailed configurations are provided in Appendix E).

Result Analysis. For **Q1**, Table 3 (full results in Appendix F.1) summarizes the zero-shot evaluation results across Image-Goal, Point-Goal, and No-Goal exploration. WAM-Nav achieves the best average performance across the three task settings, reaching 50.2% SR / 48.2% SPL on Image-Goal, 80.4% SR / 78.0% SPL on Point-Goal, and 171.1 m² explored area in No-Goal exploration. The consistent gains across both *ClutterScenes* and *InternScenes* suggest that jointly learning action generation with latent visual foresight improves zero-shot robustness under diverse obstacle layouts and semantic scene complexity. Meanwhile, the balanced performance across goal types supports the effectiveness of unified goal alignment for a single multi-task navigation policy.

For **Q2**, Figure 3 qualitatively compares NavDP and WAM-Nav on the Image-Goal task. NavDP often reacts only after approaching obstacles, causing abrupt trajectory changes in cluttered areas. In contrast, WAM-Nav uses short-horizon latent foresight to anticipate near-future geometric constraints while maintaining long-horizon action continuity, leading to smoother and more proactive obstacle avoidance. The decoded foresight remains consistent with ground-truth observations, indicating that latent foresight provides reliable guidance without requiring long autoregressive visual rollouts.

For **Q3**, Table 1 shows that WAM-Nav remains efficient for online navigation despite incorporating latent visual foresight. Although it has a larger total parameter count due to frozen visual priors, its trainable parameters are comparable to NavDP while requiring lower per-decision computation (0.7 vs. 1.3 TFLOPs). With an inference latency of 0.26 s, WAM-Nav introduces only modest overhead over NavDP, while avoiding the costly multi-candidate visual rollouts of NWM (1.43 s, 8.3 TFLOPs), validating the efficiency of asymmetric short-horizon foresight for real-time navigation.

For **Q4**, Table 4 (Appendix F.2) evaluates the roles of trajectory conditioning and latent foresight. Latent prediction alone improves SR from 42.1% to 45.7%, showing that foresight helps the policy anticipate local obstacle constraints. Motion trajectories alone improve performance in *ClutterScenes* but degrade in more semantically complex *InternScenes*, indicating that kinematic history improves smoothness but cannot replace perceptual foresight. Combining both yields the best result (50.2% SR / 48.2% SPL), supporting the DSCC design: ego-motion history stabilizes trajectory generation, while latent foresight provides the geometric constraints needed for safe navigation.

Table 1: Computational efficiency comparison across navigation methods.

Method	Inference Latency (s) ↓	Total Params	Trainable Params	TFLOPs ↓
NWM	1.43	154.4M	68.3M	8.3
NavDP	0.16	136.4M	136.4M	1.3
Ours	0.26	234.9M	129.2M	0.7

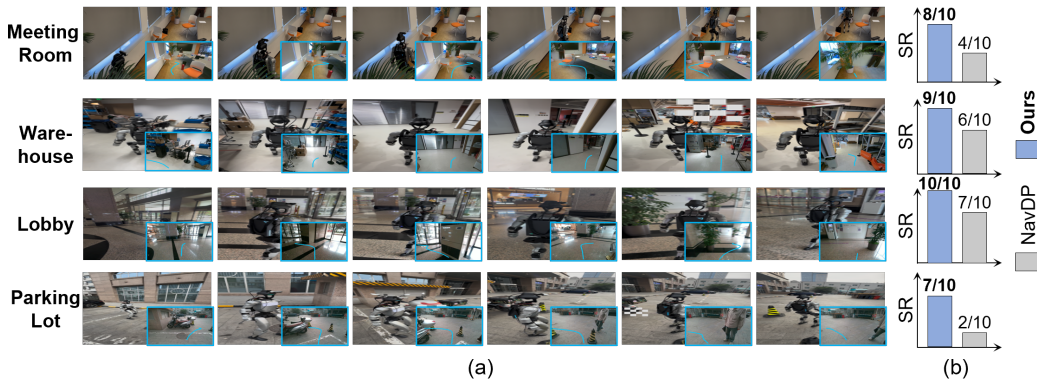


Figure 4: **Zero-shot deployment of WAM-Nav in real-world environments.** (a) Visualization of WAM-Nav navigating across four representative indoor and outdoor scenes, with the first-person trajectory planning visualization shown in the bottom-right corner of each image. (b) Quantitative comparison of WAM-Nav and NavDP in each real-world scenario.

4.2 Deployment on Real World

For **Q5**, we deploy WAM-Nav in a zero-shot manner on a real-world Unitree G1 humanoid robot equipped with an Intel RealSense D455 camera. Evaluation is conducted across four indoor and outdoor environments: a *meeting room*, *warehouse*, *lobby*, and *parking lot*, with 10 trials per scene. As shown in Fig. 4(a), WAM-Nav consistently predicts feasible trajectories under diverse layouts and lighting conditions, achieving an average 85% success rate. Compared with NavDP, the higher success rate indicates that latent foresight and motion-aware conditioning improve obstacle avoidance and trajectory stability beyond simulation, supporting effective zero-shot sim-to-real transfer.

5 Conclusion

This paper presents WAM-Nav, a Latent World-Action Model for embodied visual navigation that unifies action generation and latent visual foresight within a shared generative framework. By using asymmetric action-foresight generation, WAM-Nav preserves long-horizon trajectory continuity while avoiding the latency and error accumulation of long visual rollouts. Its dual-stream conditioning further integrates sequential visual observations with episode-level ego-motion history, guiding the policy toward trajectories that are both geometrically safe and kinematically smooth. Together with unified goal alignment, the same policy supports Image-Goal, Point-Goal, and No-Goal exploration. Extensive zero-shot experiments on *ClutterScenes* and *InternScenes*, together with real-world deployment on a humanoid robot, demonstrate strong generalization, effective sim-to-real transfer, and practical potential for robust embodied navigation.

Limitations. During real-world deployment of WAM-Nav, we identify two primary failure modes. First, the limited camera height and field of view restrict perception of near-field obstacles, which may lead to inaccurate trajectory prediction or delayed avoidance. Second, the current policy does not explicitly model robot embodiment, causing mismatches between camera-level obstacle avoidance and full-body traversability. These limitations suggest two promising future directions: adaptive viewpoint control for dynamic perception adjustment, and embodiment-aware training with diverse robot morphologies to improve navigation robustness.

References

- [1] X. Wei, C. Gu, and H. Zhu. Navol: Navigation policy with online imitation learning. *arXiv preprint*, 2026. URL <https://arxiv.org/abs/2605.11762>.
- [2] N. Yang, F. Lu, X. Li, G. Tian, Z. Li, and T. Fu. Transformer-driven semantic-spatial adaptive fusion representation for object-goal navigation. *IEEE Transactions on Automation Science and Engineering*, 22:19135–19150, 2025.
- [3] N. Yang, F. Lu, G. Tian, and J. Liu. Long-term active object detection for service robots: Using generative adversarial imitation learning with contextualized memory graph. *IEEE Transactions on Industrial Electronics*, 72(5):5082–5092, 2025.
- [4] J. Zhang, A. Li, Y. Qi, M. Li, J. Liu, S. Wang, H. Liu, G. Zhou, Y. Wu, Y. Fan, W. Li, Z. Chen, F. Gao, Q. Wu, Z. Zhang, and H. Wang. Embodied navigation foundation model. *arXiv preprint*, 2025.
- [5] F. Zhu, Y. Zhu, X. Chang, and X. Liang. Deep learning for embodied vision navigation: A survey. *arXiv preprint*, 2021.
- [6] C. Campos, R. Elvira, J. J. Gómez, J. M. M. Montiel, and J. D. Tardós. ORB-SLAM3: An accurate open-source library for visual, visual-inertial, and multimap SLAM. *IEEE Transactions on Robotics*, 37(6):1874–1890, 2021.
- [7] M. Labbé and F. Michaud. Rtab-map as an open-source lidar and visual simultaneous localization and mapping library for large-scale and long-term online operation. *Journal of Field Robotics*, 36(2):416–446, 2019.
- [8] D. S. Chaplot, D. Gandhi, S. Gupta, A. Gupta, and R. Salakhutdinov. Learning to explore using active neural SLAM. In *International Conference on Learning Representations (ICLR)*, 2020. URL <https://openreview.net/forum?id=H1IujJStpr>.
- [9] D. Shah, A. Sridhar, A. Rutishauser, X. Gao, V. Blukis, D. Hwang, and S. Levine. GNM: A general navigation model to drive any robot. In *2023 IEEE International Conference on Robotics and Automation (ICRA)*, pages 7226–7233. IEEE, 2023.
- [10] D. Shah, A. Sridhar, N. Dashora, et al. ViNT: A foundation model for visual navigation. In *Conference on Robot Learning (CoRL)*, 2023.
- [11] A. Sridhar, D. Shah, C. Glossop, and S. Levine. NoMaD: Goal masking diffusion policies for navigation and exploration. In *2024 IEEE International Conference on Robotics and Automation (ICRA)*. IEEE, 2024.
- [12] J. Peng, W. Cai, Y. Yang, T. Wang, Y. Shen, and J. Pang. Logoplanner: Localization grounded navigation policy with metric-aware visual geometry. *arXiv preprint*, 2025.
- [13] W. Cai, J. Peng, Y. Yang, Y. Zhang, M. Wei, H. Wang, Y. Chen, T. Wang, and J. Pang. NavDP: Learning sim-to-real safe navigation with diffusion policy and critic score. In *2025 IEEE International Conference on Robotics and Automation (ICRA)*. IEEE, 2025.
- [14] Y. Qin, A. Sun, Y. Hong, B. Wang, and R. Zhang. Navigatediff: Visual predictors are zero-shot navigation assistants. In *2025 IEEE International Conference on Robotics and Automation (ICRA)*, 2025.
- [15] F. Ni, J. Hao, S. Wu, L. Kou, J. Liu, Y. Zheng, B. Wang, and Y. Zhuang. Generate subgoal images before act: Unlocking the chain-of-thought reasoning in diffusion model for robot manipulation with multimodal prompts. In *Proceedings of the IEEE/CVF Conference on Computer Vision and Pattern Recognition (CVPR)*, pages 13991–14000, 2024.

- [16] A. Bar, G. Zhou, D. Tran, et al. Navigation world models. In *Proceedings of the IEEE/CVF Conference on Computer Vision and Pattern Recognition (CVPR)*, 2025.
- [17] M. Zhang, W. Shen, F. Zhang, H. Qin, Z. Pei, and Z. Meng. RAE-NWM: Navigation world model in dense visual representation space. *arXiv preprint*, 2026.
- [18] Y. Dong, F. Wu, G. Chen, Z.-Q. Cheng, Q. Hu, Y. Zhou, J. Sun, J.-Y. He, Q. Dai, and A. G. Hauptmann. Towards unified world models for visual navigation via memory-augmented planning and foresight. *arXiv preprint*, 2025.
- [19] S. Ye, Y. Ge, K. Zheng, S. Gao, S. Yu, G. Kurian, S. Indupuru, Y. L. Tan, C. Zhu, J. Xiang, T. Zhang, H. Ji, Z. Liu, K. He, S. Xie, S. Song, P. Abbeel, S. Levine, C. Finn, et al. World action models are zero-shot policies. *arXiv preprint*, 2026. URL <https://arxiv.org/abs/2602.15922>.
- [20] H. Bi, H. Tan, S. Xie, Z. Wang, S. Huang, H. Liu, R. Zhao, Y. Feng, C. Xiang, Y. Rong, Z. Li, Y. Chen, J. Zhang, Y. Li, L. Ma, Y. Qiao, et al. Motus: A unified latent action world model. *arXiv preprint*, 2025. URL <https://arxiv.org/abs/2512.13030>.
- [21] A. Group, H. K. U. of Science, and Technology. Causal world modeling for robot control. *arXiv preprint*, 2026. URL <https://arxiv.org/abs/2601.21998>.
- [22] Y. Zhu, R. Mottaghi, E. Kolve, A. Torralba, A. Gupta, L. Fei-Fei, and A. Farhadi. Target-driven visual navigation in indoor scenes using deep reinforcement learning. In *2017 IEEE International Conference on Robotics and Automation (ICRA)*, pages 3357–3364. IEEE, 2017.
- [23] M. Savva, A. Kadian, O. Maksymets, Y. Zhao, E. Wijmans, B. Jain, J. Straub, J. Liu, V. Koltun, J. Malik, et al. Habitat: A platform for embodied ai research. In *Proceedings of the IEEE/CVF International Conference on Computer Vision (ICCV)*, pages 9339–9347. IEEE, 2019.
- [24] E. Wijmans, A. Kadian, A. Morcos, S. Lee, I. Essa, D. Parikh, M. Savva, and D. Batra. DD-PPO: Learning near-perfect pointgoal navigators from 2.5 billion frames. In *International Conference on Learning Representations (ICLR)*, 2020.
- [25] Y. Zeng, H. Ren, S. Wang, J. Huang, and H. Cheng. Navidiffusor: Cost-guided diffusion model for visual navigation. In *2025 IEEE International Conference on Robotics and Automation (ICRA)*, 2025.
- [26] A. Krizhevsky, I. Sutskever, and G. E. Hinton. Imagenet classification with deep convolutional neural networks. In *Advances in Neural Information Processing Systems (NeurIPS)*, volume 25, pages 1097–1105, 2012.
- [27] M. Janner, Y. Du, J. B. Tenenbaum, and S. Levine. Policy learning via action diffusion. In *Proceedings of Robotics: Science and Systems (RSS)*, Daegu, Republic of Korea, July 2023.
- [28] W. Shen, Z. Meng, J. Ma, M. Zhou, and D. Xiang. An efficient and multi-modal navigation system with one-step world model. *arXiv preprint*, 2026. URL <https://arxiv.org/abs/2601.12277>.
- [29] H. Zhang, S. Liang, L. Chen, Y. Li, Y. Xu, Y. Zhong, F. Zhang, and H. Li. Sparse video generation propels real-world beyond-the-view vision-language navigation. *arXiv preprint*, 2026.
- [30] D. Nie, X. Guo, Y. Duan, R. Zhang, and L. Chen. Wmnav: Integrating vision-language models into world models for object goal navigation. In *2025 IEEE/RSJ International Conference on Intelligent Robots and Systems (IROS)*, 2025.
- [31] J. Y. Koh, H. Lee, Y. Yang, J. Baldridge, and P. Anderson. Pathdreamer: A world model for indoor navigation. In *Proceedings of the IEEE/CVF International Conference on Computer Vision (ICCV)*, pages 14738–14748, 2021.

- [32] J. Ho, A. Jain, and P. Abbeel. Denoising diffusion probabilistic models. In *Advances in Neural Information Processing Systems (NeurIPS)*, volume 33, pages 6840–6851, 2020.
- [33] S. Wang, Y. Wang, Z. Fan, Y. Wang, M. Chen, K. Wang, Z. Su, W. Li, X. Cai, Y. Jin, and D. Li. Internvla-n1: An open dual-system vision-language navigation foundation model with learned latent plans. *arXiv preprint*, 2025. arXiv number placeholder.
- [34] M. Oquab, T. Darcet, T. Moutakanni, H. V. Vo, M. Szafraniec, V. Khalidov, P. Fernandez, D. Haziza, F. Massa, A. El-Nouby, et al. Dinov2: Learning robust visual features without supervision. *arXiv preprint*, 2023.
- [35] R. Rombach, A. Blattmann, D. Lorenz, P. Esser, and B. Ommer. Stable diffusion v1. <https://github.com/Stability-AI/stablediffusion>, 2022.
- [36] S. Jiang, S. Ancha, N. Roy, T. Lozano-Pérez, L. P. Kaelbling, et al. Streaming flow policy: Simplifying diffusion/flow-matching policies by treating action trajectories as flow trajectories. *arXiv preprint*, 2025.
- [37] A. van den Oord, Y. Li, and O. Vinyals. Representation learning with contrastive predictive coding. *arXiv preprint*, 2018.
- [38] I. Contributors. Interndata-n1 dataset. <https://huggingface.co/datasets/InternRobotics/InternData-N1>, 2025. Accessed: 2025-09-15.
- [39] J. Straub, T. Whelan, L. Ma, Y. Chen, E. Wijmans, S. Green, J. J. Engel, R. Mur-Artal, C. Ren, S. Verma, A. Clarkson, M. Yan, B. Budge, Y. Yan, X. Pan, J. Youn, Y. Zou, N. Ratliff, D. Huang, S. Wang, F. Yang, J. J. Leonard, and J. Shen. The replica dataset: A digital replica of indoor spaces. *arXiv preprint*, 2019.
- [40] A. Chang, A. Dai, T. Funkhouser, M. Halber, M. Niebner, M. Savva, S. Song, A. Zeng, and Y. Zhang. Matterport3d: Learning from rgb-d data in indoor environments. In *2017 International Conference on 3D Vision (3DV)*. IEEE, 2017.
- [41] F. Xia, A. R. Zamir, Z.-Y. He, A. Sax, J. Malik, and S. Savarese. Gibson env: Real-world perception for embodied agents. In *Proceedings of the IEEE Conference on Computer Vision and Pattern Recognition (CVPR)*, pages 9068–9079, 2018.
- [42] H. Fu, B. Cai, L. Gao, L.-X. Zhang, J. Wang, X. Li, X. Cao, S.-Q. Han, Y.-W. Liu, O. Wang, et al. 3d-front: 3d furnished rooms with layouts and semantics. *arXiv preprint*, 2020.
- [43] M. Khanna, Y. Wang, M. Z. Irshad, T. Gervet, Y. Xu, Y. Han, C. Gan, T.-W. Lee, D. Xu, K.-L. Gervet, et al. Habitat synthetic scenes dataset (hssd-200): An analysis of 3d scene scale and realism tradeoffs for objectgoal navigation. *arXiv preprint*, 2023.
- [44] S. K. Ramakrishnan, A. Gokaslan, E. Wijmans, O. Mousavian, A. Clegg, B. Diorio, S. Song, D. Batra, J. Malik, and S. Lee. Habitat-matterport 3d dataset (hm3d): 1000 large-scale 3d environments for embodied ai. In *Thirty-fifth Conference on Neural Information Processing Systems (NeurIPS) Datasets and Benchmarks Track*, 2021.
- [45] H. Wang, J. Chen, W. Huang, Q. Ben, T. Wang, B. Mi, T. Huang, S. Zhao, Y. Chen, S. Yang, P. Cao, W. Yu, Z. Ye, J. Li, J. Long, Z. Wang, H. Wang, Y. Zhao, Z. Tu, Y. Qiao, D. Lin, and J. Pang. Grutopia: Dream general robots in a city at scale. *arXiv preprint*, 2024.
- [46] F. Yang, C. Wang, C. Cadena, and M. Hutter. iplanner: Imperative path planning. In *Proceedings of Robotics: Science and Systems (RSS)*, Daegu, Republic of Korea, July 2023.
- [47] P. Roth, J. Nubert, F. Yang, M. Mittal, and M. Hutter. Viplanner: Visual semantic imperative learning for local navigation. In *2024 IEEE International Conference on Robotics and Automation (ICRA)*. IEEE, 2024.

A Overview

The supplementary material is organized as follows:

- Section B provides the formal problem definition.
- Section C provides additional details of the proposed method.
- Section D presents the model configurations and training details of WAM-Nav.
- Section E introduces the details of the baseline methods.
- Section F includes additional experimental results and ablation studies.
- Section G describes the hardware setup and deployment details for real-world experiments.
- Section H provides the visualization of a failure case.

B Problem Definition

We consider mapless visual navigation under three goal modalities: Image-Goal (g^{img}), Point-Goal (g^{pt}), and No-Goal exploration (g^{\emptyset}). At each time step t in a partially observable environment, the agent receives a visual history $\mathcal{O}_t = \{o_{t-k+1}, \dots, o_t\}$, an action-accumulated ego-motion history $\mathcal{S}_t = \{s_{t-k+1}, \dots, s_t\}$, and a goal condition $g \in \{g^{\text{img}}, g^{\text{pt}}, g^{\emptyset}\}$.

To move beyond myopic reactive control, WAM-Nav formulates navigation as conditional asymmetric joint generation. Conditioned on the compact conditioning context C constructed from $(\mathcal{O}_t, \mathcal{S}_t, g)$, the policy predicts a long-horizon action trajectory $\mathbf{A}_t = \{a_t, \dots, a_{t+H_{\text{act}}-1}\}$ and a short-horizon latent visual foresight sequence $\mathbf{Z}_{t+1:t+H_{\text{vis}}} = \{z_{t+1}, \dots, z_{t+H_{\text{vis}}}\}$, where $H_{\text{vis}} \leq H_{\text{act}}$. The learning objective is to model:

$$p_{\theta}(\mathbf{A}_t, \mathbf{Z}_{t+1:t+H_{\text{vis}}} \mid C). \quad (9)$$

Through this formulation, long-horizon actions maintain trajectory continuity, while short-horizon latent foresight provides reliable near-future geometric constraints for safe navigation.

Algorithm 1 Online Ego-Motion History and Egocentric Conversion

Require: window length k ; executed action a_{t-1} ; pose accumulator s_{t-1} ; pose buffer \mathcal{B}

Ensure: egocentric relative-motion sequence $\tilde{\mathcal{S}}_t = \{(\Delta x_i, \Delta y_i, \Delta \theta_i)\}_{i=t-k+1}^t$

```

 $s_t \leftarrow s_{t-1} + a_{t-1}$ 
Append  $s_t$  to  $\mathcal{B}$ ; if  $|\mathcal{B}| > k$ , remove the oldest pose
if  $|\mathcal{B}| < k$  then
     $\mathcal{S}_t \leftarrow$  zero-pad the front of  $\mathcal{B}$  to length  $k$ 
else
     $\mathcal{S}_t \leftarrow \mathcal{B}$ 
end if
 $s_t = (x_t, y_t, \theta_t) \leftarrow$  the last pose in  $\mathcal{S}_t$ 
 $\tilde{\mathcal{S}}_t \leftarrow \emptyset$ 
for each  $s_i = (x_i, y_i, \theta_i)$  in  $\mathcal{S}_t$  do
     $\delta x \leftarrow x_i - x_t, \delta y \leftarrow y_i - y_t$ 
     $\Delta x \leftarrow \cos \theta_t \cdot \delta x + \sin \theta_t \cdot \delta y$ 
     $\Delta y \leftarrow -\sin \theta_t \cdot \delta x + \cos \theta_t \cdot \delta y$ 
     $\Delta \theta \leftarrow \text{atan2}(\sin(\theta_i - \theta_t), \cos(\theta_i - \theta_t))$ 
    Append  $(\Delta x, \Delta y, \Delta \theta)$  to  $\tilde{\mathcal{S}}_t$ 
end for

```

C Method Details

C.1 Trajectory-Aware Motion History

While goal-modulated visual memory provides spatial context over \mathcal{O}_t , it does not explicitly encode kinematic momentum; the motion trajectory stream therefore maintains an action-accumulated ego-motion history $\mathcal{S}_t = \{s_{t-k+1}, \dots, s_t\}$ (Sec. B). At deployment, each executed action a_{t-1} updates the current planar pose s_t , which is appended to a length- k sliding buffer and zero-padded at the front when the episode is shorter than k steps. The buffer is then re-expressed in the current egocentric frame—re-centering on s_t , rotating translations by θ_t , and wrapping heading differences—so that the stream receives a complete relative-motion sequence $\tilde{\mathcal{S}}_t = \{(\Delta x_i, \Delta y_i, \Delta \theta_i)\}_{i=t-k+1}^t$ rather than absolute scene coordinates. Algorithm 1 details this online procedure.

C.2 Architecture of the Shared DiT Block

As introduced in the **Asymmetric Action-Foresight Generation** subsection, the shared DiT predicts the joint flow-matching velocity fields \hat{u}_A and \hat{u}_Z from the interpolated action and latent visual states $(\mathbf{A}_\tau, \mathbf{Z}_\tau)$, conditioned on the conditioning context C and flow timestep τ . Figure. 5 illustrates a single DiT block, stacked N times.

At each block, \mathbf{A}_τ and \mathbf{Z}_τ are tokenized into parallel action and image streams. The timestep embedding τ is injected into each stream via separate adaLN-Zero branches. The modulated tokens then pass through a shared self-attention layer, enabling early interaction between action and latent visual tokens. After the residual update, both streams perform cross-attention over the conditioning context C using shared cross-attention and FFN weights with stream-specific modulation. The updated features are propagated through stacked blocks, and finally projected to \hat{u}_A and \hat{u}_Z . This design enables consistent action-foresight generation through shared parameters and cross-modal coupling.

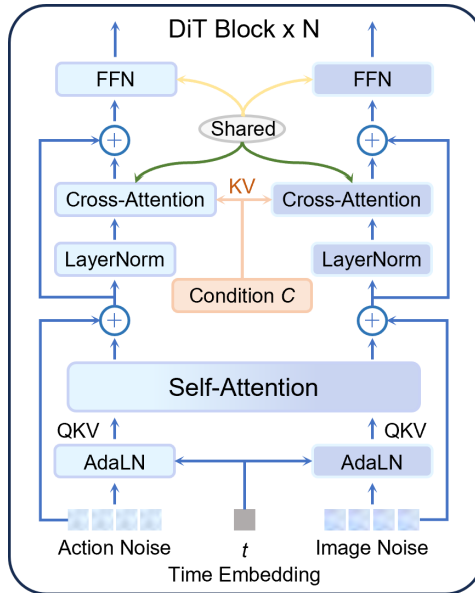


Figure 5: Architecture of the shared DiT block for asymmetric action-foresight generation. Noised action tokens and latent visual foresight tokens are modulated through separate adaLN branches, coupled via shared self-attention, and grounded on the conditioning context C through shared cross-attention and FFN layers.

Table 2: Key hyperparameters of WAM-Nav.

Parameter	Value	Parameter	Value
Hidden Dimension	384	Condition Length	64
Memory Window (k)	8	Action Horizon (H_{act})	24
DiT Layers	16	DiT Attention Heads	8
Fusion Layers	4	Fusion Attention Heads	8
Causal Layers	2	Causal Attention Heads	4
Latent Grid Size	16×16	Latent Channels	4
Image Patches	16	Dropout	0.1
Batch Size	256	Learning Rate	1.5×10^{-4}
Weight Decay	1×10^{-4}	Warmup Ratio	0.05
λ_{img}	0.25	λ_{align}	0.1
Inference Steps	10	Visual Horizon (H_{vis})	1
Visual Backbone	DINOv2 ViT-S/14	–	–

D Implementation Details of WAM-Nav

We train WAM-Nav using a batch size of 256 and optimize the model with the AdamW optimizer. The peak learning rate is set to 1.5×10^{-4} with a weight decay of 1×10^{-4} , following a cosine annealing schedule with a 5% linear warmup. During training, the visual backbone (DINOv2 ViT-S/14) and the pre-trained Stable Diffusion VAE are kept frozen to preserve their general-purpose representations, while the goal image encoder, fusion decoder, causal motion encoder, and the shared DiT are trained from scratch. The loss weighting coefficients in Eq. 8 are empirically set to $\lambda_{img} = 0.25$ and $\lambda_{align} = 0.1$. At deployment, the flow-matching ODE solver runs for $N_{steps} = 10$ Euler integration steps, which balances high-quality trajectory generation with real-time responsiveness. The detailed hyperparameter configurations are summarized in Table 2.

E Baseline Details

To comprehensively evaluate WAM-Nav, we compare against representative baselines spanning reinforcement learning, reactive planning, foundation models, and generative world models.

- **DD-PPO** [24]: A large-scale distributed reinforcement learning framework for Point-Goal navigation, trained over billions of frames in Habitat and widely adopted as a strong map-less navigation baseline.
- **iPlanner** [46]: A high-frequency local planner that directly predicts multi-step continuous trajectories through spline regression for reactive obstacle avoidance.
- **ViPlanner** [47]: An end-to-end semantic planner that predicts 2D collision cost maps from monocular observations for safe trajectory generation.
- **GNM** [9]: A general navigation foundation model trained on large-scale cross-embodiment datasets for zero-shot transfer and low-level action prediction.
- **ViNT** [10]: A Transformer-based navigation policy that extends GNM by jointly modeling heterogeneous visual navigation data with improved sequence representation.
- **NoMaD** [11]: A diffusion-based action policy that introduces goal masking to unify goal-conditioned navigation and goal-free exploration.
- **NWM** [16]: A generative navigation world model based on conditional DiT that predicts future egocentric observations for foresight-driven planning.
- **NavDP** [13]: A diffusion-based navigation policy that leverages privileged simulation priors for zero-shot sim-to-real transfer.

F Additional Experimental Results

F.1 Main Simulation Results

Table 3: Performance comparison across three navigation tasks.

Method	ClutterScenes				InternScenes				Average	
	Easy		Hard		Home		Commercial		M_1	M_2
	M_1	M_2	M_1	M_2	M_1	M_2	M_1	M_2		
Task 1: Image-Goal Navigation (M_1: SR \uparrow, M_2: SPL \uparrow)										
GNM	26.9	25.9	20.0	19.2	7.7	7.3	10.5	10.3	16.3	15.7
ViNT	15.0	13.9	16.5	15.2	6.2	6.0	12.9	12.2	12.6	11.8
NoMaD	8.3	6.9	7.3	6.9	6.7	6.2	11.7	10.7	8.5	7.6
NWM	12.7	12.0	8.7	8.4	4.0	3.9	6.9	6.6	8.1	7.7
NavDP	49.7	48.4	47.5	46.3	29.8	27.7	46.6	43.3	43.4	41.4
Ours	66.1	64.5	55.6	53.4	30.7	29.4	48.3	45.6	50.2	48.2
Task 2: Point-Goal Navigation (M_1: SR \uparrow, M_2: SPL \uparrow)										
DD-PPO	0.0	0.0	0.0	0.0	0.4	0.4	5.3	5.2	1.4	1.4
iPlanner	89.4	88.4	80.3	78.8	43.0	40.6	54.6	52.8	66.8	65.1
ViPlanner	80.2	80.1	64.7	64.5	45.0	43.2	63.7	61.9	63.4	62.4
NavDP	92.3	90.5	87.4	84.9	60.0	55.6	71.4	68.2	77.8	74.8
Ours	93.8	91.6	88.9	86.4	61.4	58.6	77.4	75.3	80.4	78.0
Task 3: No-Goal Exploration (M_1: Area \uparrow, M_2: Time \uparrow)										
GNM	42.8	17.1	29.6	12.5	19.8	30.8	19.2	28.1	27.8	22.1
ViNT	55.3	20.3	46.6	18.9	20.8	31.5	22.4	27.2	36.2	24.4
NoMaD	119.4	48.1	85.7	36.6	21.7	27.8	23.4	29.7	62.5	35.5
NavDP	315.6	112.7	274.1	106.2	34.1	35.0	43.9	36.2	167.2	72.5
Ours	320.4	115.2	281.7	108.6	36.8	38.3	45.5	40.2	171.1	75.6

F.2 Main Component Ablation

Table 4: Ablation study of different components of WAM-Nav on Image-Goal navigation.

Method		ClutterScenes (Avg.)		InternScenes (Avg.)		Overall Average	
Motion Traj.	Latent Pred.	SR	SPL	SR	SPL	SR	SPL
×	×	51.0	49.9	33.2	31.7	42.1	40.8
×	✓	57.4	55.5	34.0	32.2	45.7	43.8
✓	×	57.9	57.1	30.0	28.6	43.9	42.9
✓	✓	60.9	59.0	39.5	37.5	50.2	48.2

F.3 Additional Ablation Studies

To systematically investigate the contribution of each key component in WAM-Nav, we conduct ablation studies on unified goal alignment, dual-stream contextual conditioning, and asymmetric action-foresight generation.

For unified goal alignment, Table 6 compares variants that retain only the visual query g_V , only the geometric query g_G , or both streams. Using only g_V favors Image-Goal navigation, while using only g_G performs best on Point-Goal navigation; however, both single-stream variants become less balanced across task types. Combining g_V and g_G achieves the strongest No-Goal exploration performance and maintains competitive Image-Goal and Point-Goal results, supporting our motivation that visual-semantic and geometric goal cues are complementary for a unified multi-task policy.

To validate the remaining design choices, we conduct ablations on the Image-Goal task, including the historical memory window size (k), the DSCC fusion design, the action-foresight coupling architecture, and the visual prediction horizon. As shown in Table 5, both insufficient and excessive temporal context negatively affect navigation performance: $k = 4$ provides limited motion context,

Table 5: Ablation studies on memory window size, DSCC module, and Action-Foresight architecture.

Memory Window Size			DSCC			Action-Foresight		
Setting	SR (\uparrow)	SPL (\uparrow)	Variant	SR (\uparrow)	SPL (\uparrow)	Variant	SR (\uparrow)	SPL (\uparrow)
$k = 4$	46.6	44.1	–	–	–	Decoupled DiT	45.9	44.6
$k = 8$ (Ours)	50.2	48.2	w/o GI	44.5	42.2	Partially DiT	47.5	45.4
$k = 16$	44.9	42.3	Ours	50.2	48.2	Ours	50.2	48.2

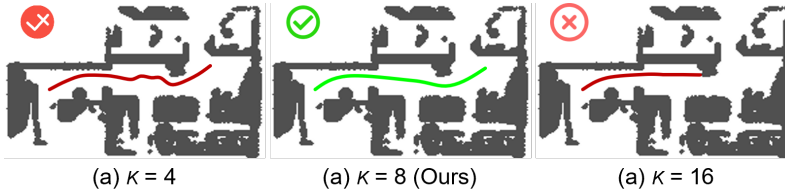


Figure 6: Visualization of the effect of different memory window sizes on navigation trajectory planning.

Table 6: Ablation study of unified goal alignment across three navigation tasks.

Variant	Image-Goal		Point-Goal		No-Goal	
	SR (\uparrow)	SPL (\uparrow)	SR (\uparrow)	SPL (\uparrow)	Area (\uparrow)	Time (\uparrow)
Only g_V	55.6	53.2	62.1	58.6	166.3	69.9
Only g_G	47.9	45.3	83.5	80.8	168.4	72.5
Ours ($g_V + g_G$)	50.2	48.2	80.4	78.0	171.1	75.6

Table 7: Ablation study of asymmetric action-foresight horizons on Image-Goal navigation.

Setting	SR (\uparrow)	SPL (\uparrow)
$H_{act} = 24, H_{vis} = 1$	50.2	48.2
$H_{act} = 24, H_{vis} = 4$	46.2	43.8
$H_{act} = 24, H_{vis} = 8$	39.6	37.3
$H_{act} = 24, H_{vis} = 24$	30.4	28.1

while $k = 16$ makes the policy less responsive to sudden geometric changes. Removing explicit goal injection (*w/o GI*) also causes a clear performance drop, confirming that goal-aware modulation is necessary for constructing effective conditioning contexts. For action-foresight coupling, the fully shared DiT outperforms decoupled and partially shared variants, indicating that latent foresight is most useful when it directly regularizes action generation through shared representations.

Table 7 further validates the asymmetric horizon design. Following NavDP, we keep the action horizon fixed at $H_{act} = 24$ to preserve long-horizon trajectory continuity, and vary the visual horizon H_{vis} . The best performance is obtained with short-horizon visual foresight ($H_{vis} = 1$), while longer visual horizons progressively degrade performance. This supports our core design motivation: in navigation, visual foresight should provide reliable near-future geometric constraints rather than long autoregressive visual rollouts, which are more prone to error accumulation under large egocentric viewpoint changes.

F.4 Comparison with NavDP

We first evaluate the zero-shot adaptability of a single WAM-Nav policy across diverse robot embodiments without any parameter retraining. As summarized in Table 8, experiments are conducted on a

Table 8: Generalization performance across different embodiments.

Embodiment	Method	Image-Goal		Point-Goal		No-Goal	
		SR (\uparrow)	SPL (\uparrow)	SR (\uparrow)	SPL (\uparrow)	Area (\uparrow)	Time (\uparrow)
Dingo	NavDP	43.4	41.4	77.8	74.8	167.2	72.5
	Ours	50.2	48.2	80.4	78.0	171.1	75.6
G1	NavDP	37.2	35.6	60.3	56.8	133.0	65.2
	Ours	42.9	42.5	64.8	63.1	147.6	68.3
H2	NavDP	32.7	31.3	47.9	46.5	142.4	67.6
	Ours	35.5	34.9	52.7	50.5	145.4	70.6

Table 9: Performance across navigation difficulty levels.

Method	Easy		Medium		Hard		Average	
	SR (\uparrow)	SPL (\uparrow)	SR (\uparrow)	SPL (\uparrow)	SR (\uparrow)	SPL (\uparrow)	SR (\uparrow)	SPL (\uparrow)
NavDP	46.2	45.7	33.8	35.6	17.4	21.3	43.4	41.4
Ours	52.5	50.5	42.4	40.5	25.0	23.8	50.2	48.2

wheeled Dingo platform together with Unitree G1 and H2 humanoid robots in the IsaacSim environment. The quantitative results demonstrate strong cross-embodiment generalization. In particular, on the G1 platform, WAM-Nav consistently outperforms NavDP across all evaluated task settings, achieving a 42.9% SR on Image-Goal navigation. On the more challenging H2 humanoid platform, WAM-Nav also achieves higher performance in all navigation tasks. These results suggest that WAM-Nav effectively learns embodiment-agnostic navigation representations, enabling stable policy transfer across robots with substantially different kinematic structures without retraining.

To further characterize the capabilities of our framework, we compare WAM-Nav and NavDP across navigation tasks of varying difficulty under the Image-Goal setting. As shown in Table 9, navigation episodes are divided into Easy, Medium, and Hard subsets according to the ground-truth path length. Across all difficulty levels, WAM-Nav consistently outperforms NavDP, with the performance gap increasing as task difficulty grows. Notably, in the Hard subset, WAM-Nav reaches 25.0% SR and 23.8% SPL, surpassing NavDP by 7.6% and 2.5%, respectively.

This growing advantage under long-horizon navigation highlights the benefit of our asymmetric action-foresight generation framework. Over extended trajectories, reactive diffusion policies such as NavDP tend to accumulate execution drift and are more vulnerable to local geometric traps due to the lack of predictive perceptual feedback. In contrast, WAM-Nav jointly models action generation and latent visual foresight, allowing near-future visual predictions to regularize trajectory planning. This coupled predictive mechanism enforces long-range spatiotemporal consistency, reduces myopic behavioral drift, and enables the policy to maintain stable and goal-directed navigation even in long-distance and cluttered environments.

G Real-World Deployment Details

G.1 Hardware setup

As shown in Figure. 7, our experimental platform is built on the Unitree G1 humanoid robot. The robot is equipped with an Intel RealSense D455 depth camera mounted on a pan-tilt servo to capture RGB-D observations from fixed viewpoints. A backpack-mounted onboard computer equipped with an RTX 4060 GPU performs real-time perception and control. A power transformer provides stable power supply for the onboard devices. This hardware setup enables real-time perception, computation, and execution for our experiments.

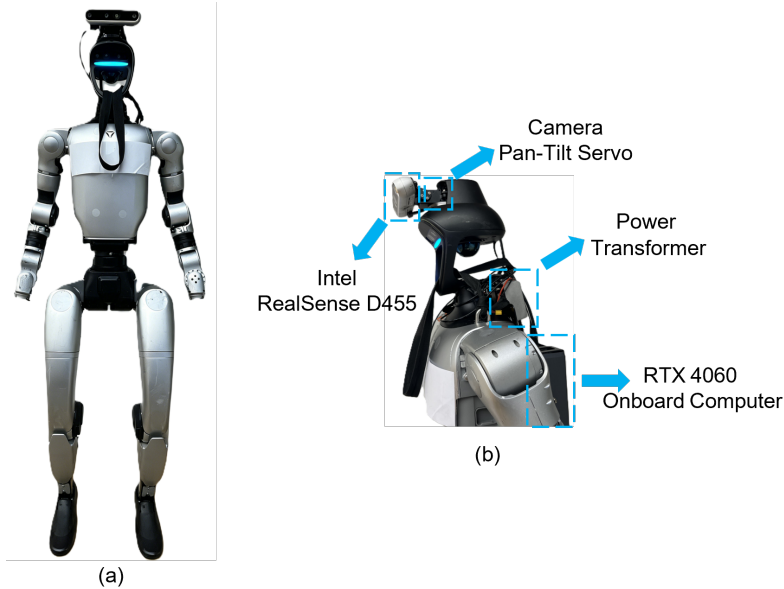


Figure 7: Robot Setup. (a) Unitree G1. (b) Detailed view of the hardware components.

G.2 Deployment Details

During deployment, the Intel RealSense D455 depth camera is mounted on the pan-tilt servo and configured with a 20° downward pitch angle to improve the observation of ground-level obstacles. The camera captures RGB-D observations at 30 Hz. The WAM-Nav model is deployed as a server on the backpack-mounted onboard computer equipped with an RTX 4060 GPU for online inference. The model occupies approximately 1.3 GB of GPU memory, and the inference frequency is set to 1 Hz. The client module is also deployed on the onboard computer. It is responsible for forwarding the incoming observations to the server and receiving the predicted outputs. The predicted trajectories are tracked using Model Predictive Control (MPC), which further converts them into velocity commands for the robot motors. During experiments, the control loop runs at 50 Hz, with each command applied for 0.1 s.

H Additional Failure Case Analysis

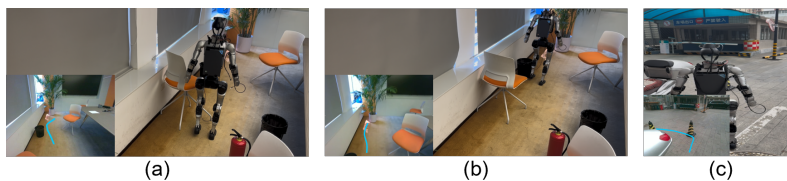


Figure 8: Failure Cases. The bottom-left subfigure shows the first-person view of the planned trajectory

In Figure 8, we visualize several typical failure cases. Case (a) shows that when the robot is close to a low obstacle, the limited field of view results in a weak perception of the obstacle, causing the robot to overlook it and eventually collide. Another common type of failure is illustrated in (b) and (c): when obstacles are located on the left or right side of the robot, the robot's body shape is not taken into account. As a result, trajectory planning only ensures that the camera can pass through, leading to collisions between the robot and the obstacles.